Determination of nanotubes properties by Raman spectroscopy

BY A. JORIO[1], R. SAITO[2], G. DRESSELHAUS[3] AND M. S. DRESSELHAUS[3]

[1] *Departamento de Física, Universidade Federal de Minas Gerais, Caixa Postal 702, Av. Antônio Carlos 6627, Belo Horizonte-MG 30123-970, Brazil* (adojorio@fisica.ufmg.br)
[2] *Department of Physics, Tohoku University and CREST JST, Aramaki, Aoba Sendai 980-8578, Japan*
[3] *Massachusetts Institute of Technology, 77 Massachusetts Avenue, Room 13-3005, Cambridge, MA 02139-4307, USA*

The basic concepts and characteristics of Raman spectra from single-wall carbon nanotubes (SWNTs, both isolated and bundled) are presented. The physical properties of the SWNTs are introduced, followed by the conceptual framework and characteristics of their Raman spectra. Each Raman feature, namely the radial breathing mode, the tangential G band, combination modes and disorder-induced bands are discussed, addressing their physical origin, as well as their capability for characterizing SWNT properties.

Keywords: carbon nanotubes; Raman spectra; one-dimensional system; electronic structure; phonons

1. Introduction

Since the first observation of carbon nanotubes, in 1991 (Iijima 1991), as multi-wall carbon nanotubes (MWNTs), and in 1993 (Bethune *et al.* 1993; Iijima & Ichihashi 1993) as single-wall carbon nanotubes (SWNTs), Raman spectroscopy has been used to characterize the synthesis and purification processes of carbon nanotubes (Dresselhaus *et al.* 2001; Journet *et al.* 1997; Tohji *et al.* 1996), as well as their physical properties. However, it was not until 1997 that the power of Raman spectroscopy for studying and characterizing carbon nanotubes started to be appreciated. Rao *et al.* (1997*a*) first demonstrated the dependence on the laser excitation energy, E_{laser}, which results from the diameter-selective resonance Raman scattering from the vibrational modes in carbon nanotubes. In 1998 Pimenta *et al.* (1998) showed that Raman spectra could be used to differentiate between metallic and semiconducting SWNTs. In 2001, it was established that resonance Raman spectra could be observed at the single-nanotube level (Jorio *et al.* 2001*a*). In combination with the unique one-dimensional (1D) electronic structure and strong electron–phonon coupling of SWNTs under resonance conditions, Raman scattering experiments at the single-nanotube level allow one to identify the nanotube structure, including its

© 2004 The Royal Society

diameter d_t and chiral angle θ, and to obtain much detailed information about the vibrational and electronic properties of nanotubes. The confinement of electrons and phonons in a 1D structure gives rise to an unexpected Raman line-shape dependence on E_{laser}, interesting effects such as Stokes/anti-Stokes asymmetry, and many phenomena not previously observed in other systems.

In this paper, the basic concepts and characteristics of Raman spectra from single-wall carbon nanotubes, both isolated and bundled (see figure 1) are presented. Section 2 discusses the physical properties of the SWNTs. The following sections discuss, separately, the Raman features allowed in a first-order Raman scattering process, originating from a single-resonance process and the combination or disorder-induced modes, which originate from the double-resonance process. Each Raman feature, namely the radial breathing mode (RBM), the tangential G band, the combination modes and disorder-induced bands, are discussed, and their physical origin and their capability for characterizing the remarkable vibrational and electronic properties of SWNTs are addressed. Raman spectra from aligned 0.4 nm diameter SWNTs inside the pores of zeolite templates and from MWNTs are presented at the end, together with a discussion on what can be learned about graphite using the Raman spectra of SWNTs.

2. Physical properties of SWNTs

The Raman spectra of carbon nanotubes consist of a rich set of features (see figure 1) with an intricate dependence on the laser energy E_{laser}, and careful spectral analysis gives detailed information on both their vibrational and electronic structures. Usually Raman spectra only explicitly involve phonons, being independent of the electronic structure of the material and the laser energy used to excite the Raman spectra. However, the scattering efficiency becomes larger when E_{laser} matches the energy between optically allowed electronic transitions in the material, in the so-called resonance Raman scattering effect (Martin & Falicov 1983). The resonance Raman intensity depends on the density of electronic states (DOS) available for the optical transitions, and this property is especially important for 1D systems, as discussed below.

An SWNT is constructed by rolling up a graphene layer into a seamless cylinder. Therefore, carbon nanotubes are strongly related to their parent material, graphite, which exhibits interesting higher-order and defect-induced Raman bands, not usually seen in typical Raman spectra of solids. It is, therefore, fruitful to develop a joint study searching for similarities between the Raman spectra of graphite and nanotubes, and for differences in these spectra related to the 1D structure of nanotubes.

(a) Unit cell of SWNTs

The nanotube structure is uniquely determined by the chiral vector C_h, which spans the circumference of the SWNT cylinder. The chiral vector can be written in the form $C_h = na_1 + ma_2 = (n, m)$, where the vectors a_1 and a_2 bounding the unit cell of the graphene layer are shown in figure 2a. The (n, m) notation (n and m are integers) is widely used to characterize the geometry of each distinct (n, m) nanotube. The nanotubes are classified as chiral ($0 < m < n$) and achiral ($m = 0$ or $m = n$), and the achiral SWNTs in turn are known as zigzag ($m = 0$) and armchair ($m = n$) nanotubes.
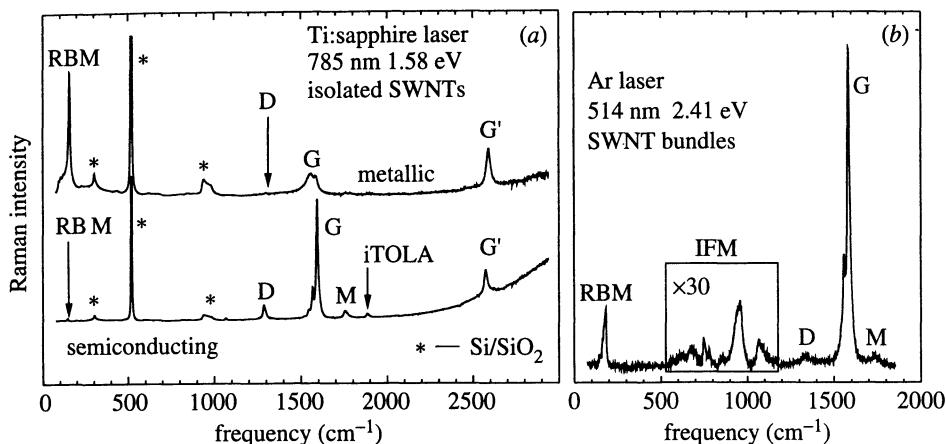
Figure 1. (*a*) Raman spectra taken at 1.58 eV from one metallic and one semiconducting SWNT grown by the CVD method on an Si/SiO$_2$ substrate. The first-order single-resonance RBM and G band features are the most intense Raman peaks. Many other harmonics and combination modes (i.e. iTOLA, M, G′) are observed, as well as disorder-induced bands (e.g. D band). The peaks marked with an '*' come from the Si/SiO$_2$ substrate. Relatively high laser powers (up to 40×10^9 W m^{-2}) can be used to probe isolated SWNTs because of the unusually high thermal conductivity values for carbon nanotubes (3000 W mK^{-1}) (Berber *et al.* 2000; Kim *et al.* 2001; Small *et al.* 2003), their excellent high-temperature stability, and their good thermal contact with the substrate. (*b*) Raman spectra taken at 2.41 eV from an SWNT bundle sample grown by the arc method. The intensity for the intermediate frequency mode (IFM) region is multiplied by 30 to clearly show the richness of the Raman spectra. The power used to measure the Raman spectra for SWNT bundles without burning the sample should be much lower than for isolated SWNTs, usually not higher than 1 mW using a 100× objective lens.
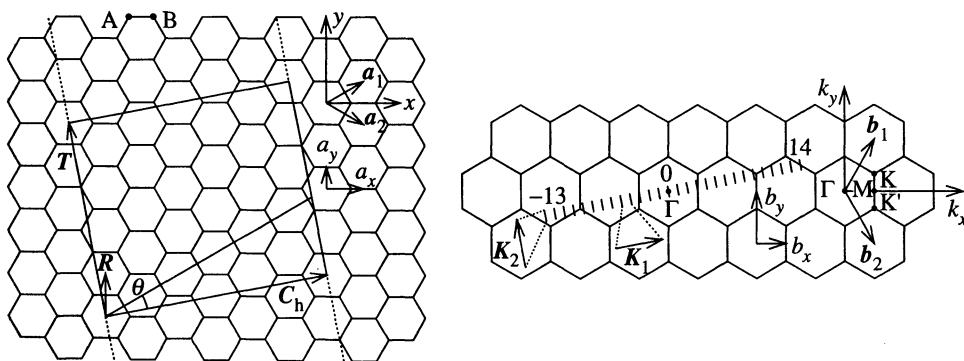
Figure 2. (*a*) Unit cell for a (4, 2) SWNT formed from a graphene layer. The chiral vector C_h is given by $C_h = 4a_1 + 2a_2$. A (4, 2) nanotube is one of the smallest-diameter nanotubes ever synthesized (Wang *et al.* 2000). (*b*) Reciprocal space of the graphene layer. Parallel equidistant lines represent the cutting lines for the (4, 2) nanotube, labelled by the cutting line index μ, which assumes values from $1 - N/2 = -13$ to $N/2 = 14$. The reciprocal lattice unit vectors (K_1, K_2) of the nanotube (shown in close-up) are indicated (Samsonidze *et al.* 2003*a*).

The unit cell of an unrolled nanotube on a graphene layer is a rectangle bounded by the vectors C_h and T (see the rectangle shown in figure 2*a* for the (4, 2) nanotube). The nanotube unit cell projected on the graphene layer consists of N hexagons

bounded by the vectors C_h and T as shown in figure 2a. The translation vector T is given by

$$T = \frac{\sqrt{3}\hat{z} \times C_h}{d_R} = \frac{(2m+n)a_1}{d_R} - \frac{(2n+m)a_2}{d_R},$$

where $\hat{z}$ is a unit vector normal to the graphene sheet and $d_R = \gcd(2n+m, 2m+n))$†.

The nanotube diameter d_t and chiral angle θ, which determine the length L of the chiral vector $C_h = |C_h| = \pi d_t \equiv L$ and the orientation of C_h on the graphene layer (see figure 2a) can both be expressed in terms of the indices n and m by the relations

$$d_t = \frac{a\sqrt{n^2 + nm + m^2}}{\pi} \quad \text{and} \quad \tan\theta = \frac{\sqrt{3}m}{2n+m},$$

as one can derive from figure 2a, where $a = \sqrt{3}a_{C-C} = 0.246$ nm is the lattice constant for the graphene layer and $a_{C-C} = 0.142$ nm is the nearest neighbour C–C distance (Saito *et al.* 1998).

(b) *Reciprocal space of SWNTs*

When a slice of graphene sheet is rolled up to form a carbon nanotube, the wave vectors along the circumferential direction become quantized due to periodic boundary conditions ($k_\perp = \ell K_1$, where $K_1 = 2/d_t$ and $\ell = 1, \ldots N$, where $N = 2(n^2 + m^2 + nm)/d_R$), while the wave vectors $k_\parallel$ along the tube-axis direction K_2 remain quasi-continuous. The resulting lines of permitted wave vectors in the reciprocal space of the SWNT can be represented in the two-dimensional (2D) graphene-sheet Brillouin zone by *cutting lines* of allowed wave vectors, as shown in figure 2b (Samsonidze *et al.* 2003a).

The reciprocal space vectors for the nanotube, K_1 and K_2, can be constructed using the standard definition, $C_h \cdot K_1 = T \cdot K_2 = 2\pi$ and $C_h \cdot K_2 = T \cdot K_1 = 0$. The vector K_2 is directed along the nanotube axis, so that the cutting lines are also aligned along the tube axis. K_1 can be written in the form $K_1 \propto t_2 b_1 - t_1 b_2$ to provide its orthogonality to the vector T, taking into account that $a_i \cdot b_j = 2\pi\delta_{ij}$. Similarly, $K_2 \propto mb_1 - nb_2$ is orthogonal to C_h. The normalization conditions $C_h \cdot K_1 = T \cdot K_2 = 2\pi$ are used to calculate the proportionality coefficients, yielding the magnitudes of the reciprocal lattice vectors,

$$|K_1| = \frac{2}{d_t} \quad \text{and} \quad |K_2| = \frac{2\pi}{|T|}.$$

The length and orientation of each cutting line in reciprocal space is given by the wave vector K_2, while the separation between two adjacent cutting lines is given by the wave vector K_1. In the case of the $(4, 2)$ nanotube, the $N = 28$ cutting lines are shown in figure 2b and are numbered by the index μ varying from $1 - N/2 = -13$ to $N/2 = 14$, where the middle cutting line $\mu = 0$ crosses the Γ point, the centre of the first Brillouin zone of the graphene layer.

(c) *Electronic structure and selection rules for optical transitions*

The electronic structure of a carbon nanotube can be obtained from its parent material, graphite, accounting for quantum confinement of the electronic states in

---

† $\gcd(k, l)$ denotes the greatest common division of the integers k and l
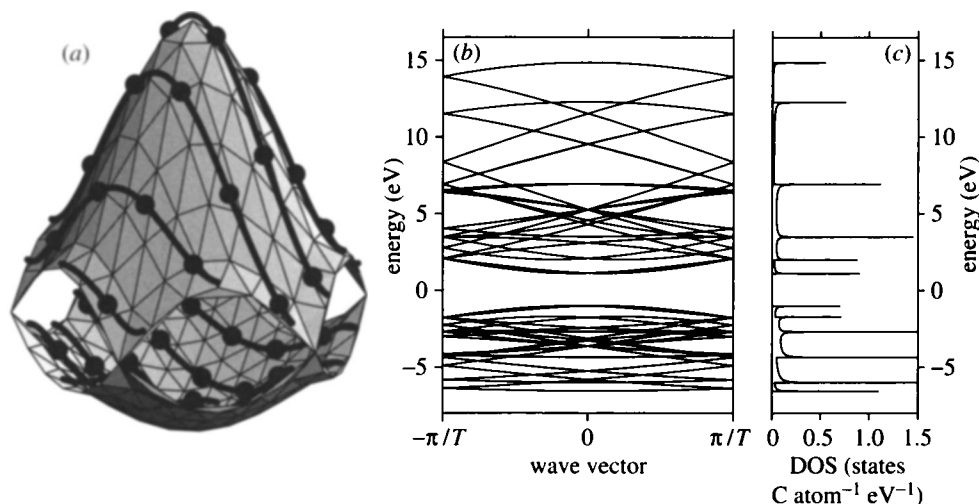
Figure 3. (a) The conduction and valence bands of the graphene layer in the first Brillouin zone calculated according to the π band nearest-neighbour TB model (Saito *et al.* 1998). Solid curves show the cutting lines for the $(4, 2)$ nanotube (Samsonidze *et al.* 2003a). (b) Band diagram for the $(4, 2)$ nanotube obtained by zone-folding from (a). (c) Density of electronic states for the band diagram shown in (b).

these 1D materials. The electronic σ bands are responsible for the strong in-plane covalent bonds within the 2D graphene sheets, while the π bands are responsible for weak van der Waals interactions between such sheets in graphite. In contrast to the σ bands, the π bands get close to the Fermi level at the K(K′) points in the Brillouin zone (see figure 2b), so that electrons can be excited from the valence (π) to the conduction (π^*) band optically. Figure 3a shows the electronic dispersion for the π and π^* bands of 2D graphite in the first Brillouin zone obtained with the tight-binding (TB) method (Saito *et al.* 1998).

The electronic band structure of the nanotube can be easily obtained by super-imposing the 1D cutting lines on the 2D electronic constant energy surfaces, as shown in figure 3a, where the cutting lines shown in figure 2b were translated to the first Brillouin zone in a K_2-extended representation (Samsonidze *et al.* 2003a). The SWNT electronic structures in figure 3a, b are given for a $(4, 2)$ SWNT (diameter $d_t = 0.4$ nm), which is used here for illustrative purposes. For such a small d_t SWNT, however, the large curvature of the graphene sheet induces changes in the C–C bond distances and causes a mixing of the σ and π bonds, and more accurate methods than TB with a nearest-neighbour interaction must be used to describe the electronic structure for small-diameter SWNTs ($d_t < 1$ nm).

The cutting line $\mu = 0$ crossing the Γ point of the graphene sheet belongs to the totally symmetric irreducible representation A. In general, the next cutting lines ($\mu = 1, 2, 3, \dots$) belong to doubly degenerate $E_1, E_2, E_3, \dots$ irreducible representations, and are related to the wave harmonics along the nanotube circumference, their eigenvectors exhibiting $2, 4, 6, \dots$ nodes, respectively.

The unique optical properties observed in SWNTs are related to their 1D confinement of electronic states, resulting in van Hove singularities (VHSs) in the DOS. Although the 1D electronic band structure of this small-diameter tube, shown in fig-
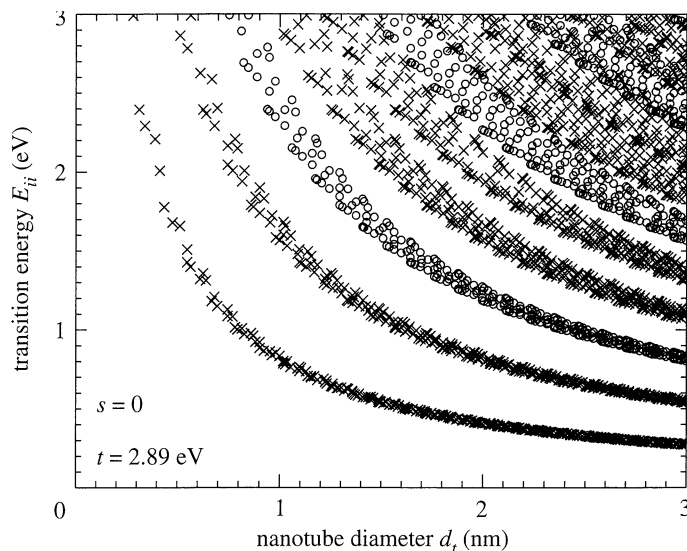
Figure 4. Electronic transition energies E_{ii} for all the (n, m) SWNTs with diameters from 0.4 nm to 3.0 nm, using a simple first-neighbour TB model (Saito *et al.* 1998). Deviations from this simple one-electron model are expected due to curvature and many-body effects.

ure 3*b*, appears to be complex, it becomes clear when considering the DOS, as shown in figure 3*c*, that the optical absorption or emission rate in SWNTs is related primarily to the electronic states at the VHSs, thereby greatly simplifying the analysis of the optical experiments.

These singularities in the DOS, and correspondingly in the joint density of states (JDOS), are of great relevance for the resonance Raman scattering of SWNTs. Whenever the energy of incident photons matches a VHS in the JDOS for the joint valence and conduction bands (subject to selection rules for optical transitions), one expects to find resonant enhancement of the corresponding Raman process. Owing to the divergent character of VHSs in these one-dimensional systems, such enhancement can be extremely confined in energy, appearing almost like the sharp transitions that are excited in a molecular system.

In spite of the large number of VHSs in the valence and conduction bands (see figure 3*c*), very few optical transitions are allowed, because of symmetry restrictions. The selection rules governing the optical transitions are commonly derived from group theory and, for light polarized parallel to the nanotube axis, only transitions between the valence and conduction subbands ($E_\mu^v \leftrightarrow E_{\mu'}^c$) belonging to the same cutting line ($\mu' = \mu$) in reciprocal space (see figure 3) are dipole allowed. Light polarized perpendicular to the nanotube induces optical transitions between adjacent cutting lines ($\mu' = \mu \pm 1$), but they are much weaker due to a depolarization effect that screens optical absorption and emission of light in such a geometry (Ajiki & Ando 1994; Marinopoulos *et al.* 2003).

Each (n, m) SWNT exhibits a different set of VHSs in its valence and conduction bands, and a different set of electronic transition energies between valence E_μ^v and conduction $E_{\mu'}^c$ band VHSs. For the characterization of nanotubes by Raman spectroscopy, it is useful to consider plots of the optically allowed transition energies for light polarized along the nanotube axis, $E_{\mu\mu}$, versus the nanotube diameter,
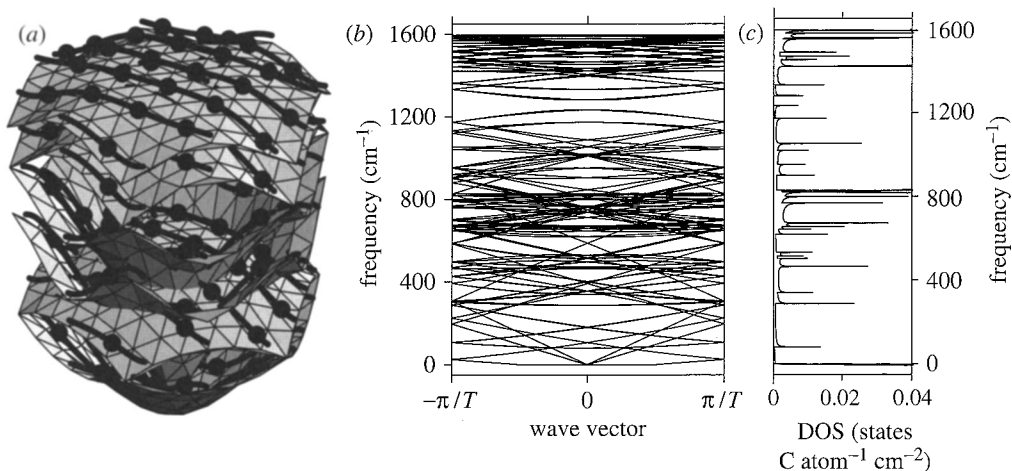
Figure 5. (*a*) The phonon dispersion relations of the graphene layer in the first Brillouin zone calculated with the force constants fitted to the Raman scattering data for various graphitic materials (Grüneis *et al.* 2002). Solid curves show the cutting lines for the $(4, 2)$ nanotube in the fully reduced representation. Solid dots show the ends of the cutting lines in the $\boldsymbol{K}_2$-extended representation. (*b*) Phonon modes versus wave vector for the $(4, 2)$ nanotube obtained by zone folding from (*a*). (*c*) Density of states for the phonon modes shown in (*b*).

d_t, as shown in the so-called Kataura plot of figure 4 (Kataura *et al.* 1999). The transition energies are labelled as E_{ii}, the subscript $i = 1, 2, 3 \ldots$ labelling the transition energy values for a given SWNT as their energy magnitude increases (Saito *et al.* 1998). SWNTs can be classified in three different families according to whether $\mathrm{mod}(2n + m, 3) = 0, 1$ or 2, where the integers $0, 1, 2$ denote the remainders when $(2n + m)$ is divided by 3. Here $\mathrm{mod}\,1$ (type 1) and $\mathrm{mod}\,2$ (type 2) SWNTs are semiconducting. $\mathrm{mod}\,0$ SWNTs $(n < m)$ are metallic at room temperature, exhibiting a small (of the order of millielectronvolts) chirality-dependent gap (quasi-metallic) at lower temperatures, while $n = m$ armchair tubes are truly metallic. Frequently, superscripts 'S' or 'M' are used to denote the electronic transition energies E_{ii}^{M} for metallic SWNTs and E_{ii}^{S} for semiconducting SWNTs. Each point in the Kataura plot represents one optically allowed electronic transition energy (E_{ii}) from a given (n, m) SWNT. Crosses denote semiconducting SWNTs, and circles denote metallic SWNTs. This plot should be considered as a guide for analysing SWNT Raman spectra.

(*d*) *Phonon structure of SWNTs*

A zone-folding picture, similar to figure 3 for electrons, gives good insights into the 1D structure of phonons in SWNTs. Two atoms 'A' and 'B' in the unit cell of the graphene layer (see figure 2*a*) give rise to six phonon modes, because of the three degrees of freedom per atom. Figure 5*a* shows a 2D representation of the six phonon branches in the first Brillouin zone (Samsonidze *et al.* 2003*a*). Superimposing the N cutting lines in the $\boldsymbol{K}_2$-extended representation on the six phonon frequency surfaces in the reciprocal space of the graphene layer, according to the zone-folding scheme as described in § 2*c*, yields $6N$ phonon modes for each carbon nanotube (see figure 5*b*). The $6(N/2 - 1)$ pairs of phonon modes arising from the cutting lines with

indices μ and $-\mu$, where $\mu = 1, \ldots, (N/2 - 1)$, are expected to be doubly degenerate, similar to the case of the electronic subbands discussed in § 2 c, while the phonon modes arising from the cutting lines with indices $\mu = 0$ and $\mu = N/2$ are non-degenerate, so the total number of distinct phonon branches is $3(N + 2)$. For the $(4, 2)$ nanotube, there are 90 distinct phonon branches, as shown in figure 5b.

Similar to electrons, phonons belonging to the cutting line $\mu = 0$, which crosses the Γ point of the graphene sheet, belong to the totally symmetric irreducible representation A. Phonons belonging to the next cutting lines ($\mu = 1, 2, 3, \ldots$) belong to double degenerate $E_1, E_2, E_3, \ldots$ irreducible representations, and are related to the wave harmonics along the nanotube circumference.

However, the zone-folding scheme neglects the curvature of the nanotube wall, and it is not accurate for the low-frequency phonon modes (zone-centre acoustic modes), while it does provide reliable results for the high-frequency phonon modes (optical modes). The zone-folding scheme predicts zero frequencies for the perfectly symmetric radial breathing mode (RBM) and twist phonon mode of the nanotube at the centre of the Brillouin zone, since they arise from the acoustic phonon modes of the graphene layer. Meanwhile, the frequency of the perfectly symmetric RBM for an isolated SWNT is inversely proportional to the nanotube diameter, varying from *ca.* 100 to 250 cm^{-1} for typical diameters of 1–2 nm, as was first predicted within the force constant model (Jishi *et al.* 1993).

In order to avoid the limitations of the zone-folding scheme for the low-frequency phonon modes, the force constant model can be used directly for nanotubes by constructing and solving the $6N \times 6N$ dynamical matrix for the unit cell of the nanotube, instead of using the 6×6 dynamical matrix for the unit cell of the graphene layer with consequent zone-folding (Saito *et al.* 1998). Alternatively, first-principles methods can be used instead of force constant models to calculate the phonon modes, but in this case the size of the unit cell should not be too large for *ab initio* methods. More details about phonon dispersion relations of carbon nanotubes can be found in Kresse (2003). Also, at the present time, the accuracy in energy resolution of Raman experiments significantly exceeds what *ab initio* calculational methods can presently achieve.

Spikes (or VHSs) appear in the density of phonon states of the SWNTs (see figure 5c), similar to the VHSs appearing in the electronic DOS, except for a much larger number of spikes in the phonon DOS than in the electronic DOS, due to the larger number of phonon modes relative to the number of electronic bands, and the more complex structure of the dispersion relations for phonons than for electrons in the graphene layer.

3. First-order single-resonance Raman spectroscopy

The first-order single-resonance Raman scattering process involves the following steps: light absorption, scattering by a phonon and light emission. The Raman signal for a given SWNT is sufficiently enhanced when either the incident or the scattered photon energy matches a VHS E_{ii} in the JDOS (see figure 4), so that, under strongly resonance conditions, the spectrum from just one nanotube can be observed. When Raman spectra of SWNT bundle samples are taken, only those SWNTs with E_{ii}
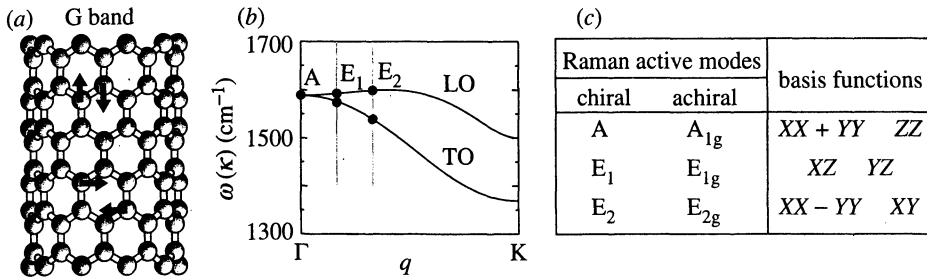
(*a*)   G band   (*b*)   (*c*)

Figure 6. (*a*) Schematic of the G band atomic vibrations along the nanotube circumference and along the nanotube axis. (*b*) The Raman active modes of A, E_1 and E_2 symmetries come from the interception of the corresponding cutting lines $\mu = 0$, $\mu = \pm1$ and $\mu = \pm2$ with the dispersion relation in the unfolded 2D Brillouin zone. The Γ points of the cutting lines are shown by solid dots. (*c*) The table gives irreducible representations and basis functions for the Raman active modes according to group theory. The Z-axis is parallel and the (X,Y)-plane is perpendicular to the nanotube axis.

in resonance with the laser excitation energy E_{laser} will contribute strongly to the spectrum. Because of the resonance process, Raman spectra allow us to study the electronic and phonon structure of SWNTs in great detail. Momentum conservation requires only phonons at the centre of the Brillouin zone (wave vector $q \approx 0$) to participate in the first-order scattering process.

This section begins with a summary of the symmetry selection rules and then discusses the two strongest features in the Raman spectra of SWNTs, namely the RBM and the graphite-like G band, which are the main Raman features used for the characterization of SWNTs. The strong RBM and the G band features appear in the Raman spectra through a first-order resonance Raman process.

(*a*) Selection rules

There are five classes of permitted first-order resonance Raman scattering processes between the VHSs E_μ^v and $E_{\mu'}^c$ (Jorio *et al.* 2003):

$$
\left.
\begin{aligned}
\text{(I)} \quad & E_\mu^v \xrightarrow{Z} E_\mu^c \xrightarrow{A} E_\mu^c \xrightarrow{Z} E_\mu^v, \\
\text{(II)} \quad & E_\mu^v \xrightarrow{X} E_{\mu\pm1}^c \xrightarrow{A} E_{\mu\pm1}^c \xrightarrow{X} E_\mu^v, \\
\text{(III)} \quad & E_\mu^v \xrightarrow{Z} E_\mu^c \xrightarrow{E_1} E_{\mu\pm1}^c \xrightarrow{X} E_\mu^v, \\
\text{(IV)} \quad & E_\mu^v \xrightarrow{X} E_{\mu\pm1}^c \xrightarrow{E_1} E_\mu^c \xrightarrow{Z} E_\mu^v, \\
\text{(V)} \quad & E_\mu^v \xrightarrow{X} E_{\mu\pm1}^c \xrightarrow{E_2} E_{\mu\mp1}^c \xrightarrow{X} E_\mu^v,
\end{aligned}
\right\}
\tag{3.1}
$$

where A, E_1, and E_2 denote phonon modes of different symmetries of the cutting lines $\mu = 0$, $\mu = \pm1$, and $\mu = \pm2$, respectively, near the Γ-point (Damnjanović *et al.* 1999; Saito *et al.* 1998, 2001). The (X, Z)-plane is parallel to the substrate on which the nanotubes lie, the Z-axis is directed along the nanotube axis, and the Y-axis is directed along the light propagation direction, so that the Z and X in equation (3.1) stand for the light polarized parallel and perpendicular to the nanotube axis, respectively. The five processes of equation (3.1) result in different polarization configurations for different phonon modes, ZZ and XX for A, ZX and
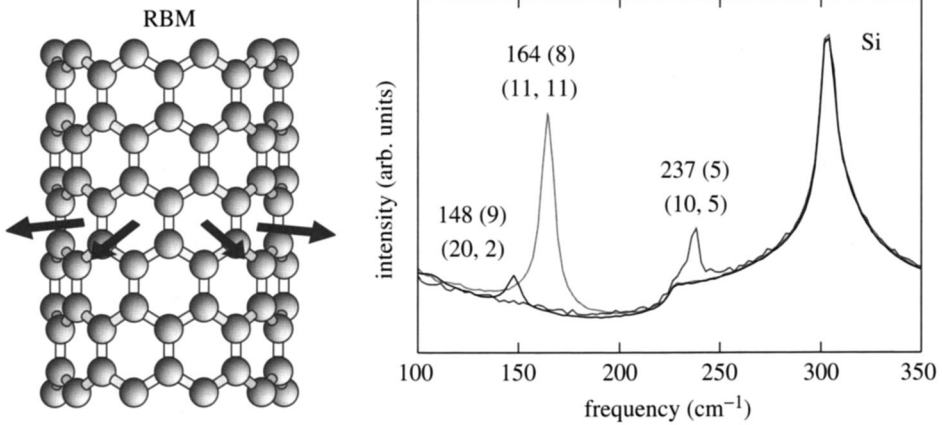
Figure 7. Schematic of the atomic vibrations in the RBM mode and Raman spectra of isolated SWNTs grown by the CVD method on an Si/SiO_2 substrate (Jorio *et al.* 2001*a*). The spectra are taken at three different spots on the substrate where the RBM Raman signal from resonant SWNTs are found. The RBM frequencies (line widths) are displayed in cm^{-1}. Also shown are the (n, m) indices assigned from the Raman spectra for each resonant tube. The step at $225\ cm^{-1}$ and the peak at $303\ cm^{-1}$ come from the Si/SiO_2 substrate.

XZ for E_1, and XX for E_2, in agreement with the basis functions predicted by group theory as discussed below in connection with the table in figure 6. Among the large number of phonon modes in carbon nanotubes, only up to 16 are Raman active (A, E_1 and E_2 symmetry modes), as predicted by group theory (Alon 2001; Dresselhaus & Eklund 2000). Also, equation (3.1) predicts *different* resonance conditions for *different* phonon modes. While the A and E_1 modes can be observed in resonance with both the $E_{\mu\mu}$ and $E_{\mu,\mu\pm1}$ VHSs in the JDOS, the E_2 modes can only be observed in resonance with the $E_{\mu,\mu\pm1}$ VHSs.

(b) The radial breathing mode

As suggested by the name, in the RBM all the C atoms are vibrating in the radial direction with the same phase (totally symmetric A mode), as if the tube were breathing (see figure 7). This Raman feature is very useful for characterizing nanotube diameters through the relation

$$\omega_{\mathrm{RBM}} = \frac{A}{d_{\mathrm{t}}},$$

where the $A = 248\ cm^{-1}$ nm parameter has been determined experimentally within 5% accuracy for isolated SWNTs on an Si/SiO_2 substrate (Jorio *et al.* 2001*a*).

Figure 7 shows the Raman spectra at three different spots on an Si/SiO_2 substrate where resonant SWNTs were observed. The step at $225\ cm^{-1}$ and the peak at $303\ cm^{-1}$ come from the Si/SiO_2 substrate, while the three peaks at 148, 164 and $237\ cm^{-1}$ are RBM features from three different (n, m) SWNTs, as assigned in figure 7. The (n, m) assignment is possible by identifying two tube properties, i.e. their diameter (from ω_{RBM}) and the resonant electronic transition energy E_{ii}, as discussed below.
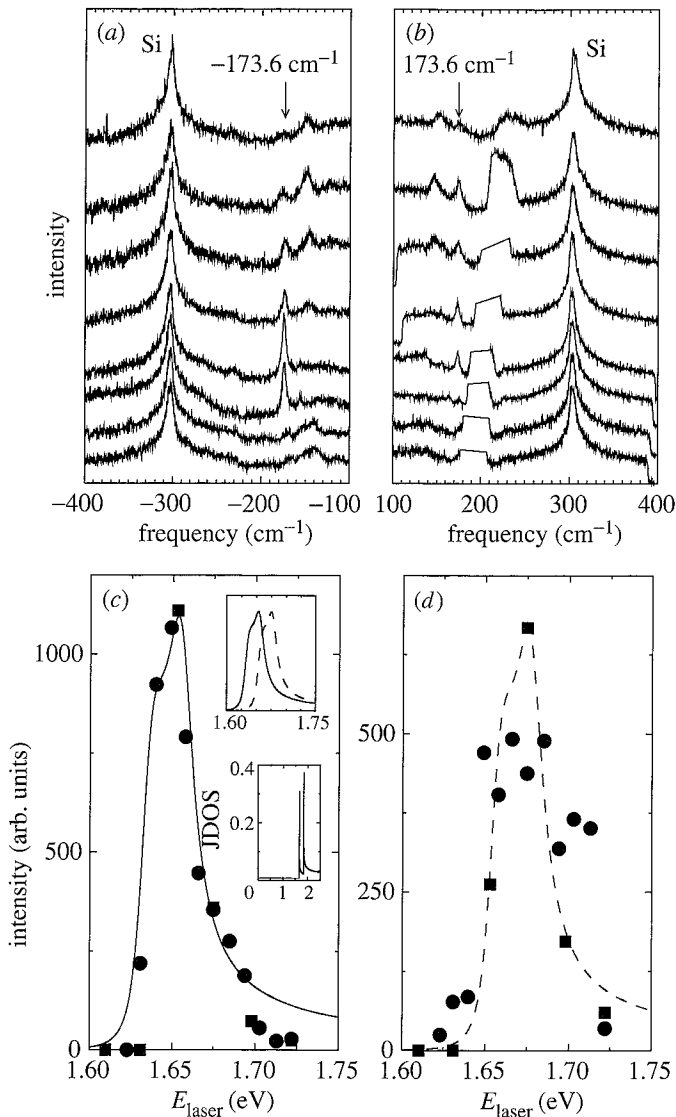
Figure 8. (*a*) The E_{laser} dependence of the anti-Stokes Raman spectra from an SWNT grown on an Si/SiO$_2$ substrate using the CVD method. The spectra from bottom to top were taken by varying E_{laser} from 1.623 eV up to 1.772 eV. The peak at ± 303 cm^{-1} comes from the substrate and was used for calibration of the Raman signal. The peak at ± 173.6 cm^{-1} is related to the RBM from an SWNT. It appears and disappears as the laser is tuned to achieve resonance. (*c*) Resonance profile (RBM intensity versus E_{laser}) for the anti-Stokes RBM spectra shown in (*a*). (*d*) Resonance profile for the Stokes spectra (shown in (*b*)). The Stokes signal is noisier because the scattered light energy falls in the range where the spectrometer gratings are losing efficiency. The solid and dashed lines in (*c*) and (*d*) are fitted to experimental points (see text). The upper inset in (*c*) shows the Stokes and anti-Stokes fitting curves together. The lower inset to (*c*) shows the sharp JDOS obtained to reproduce the fit in (*c*) and (*d*) (Jorio *et al.* 2001*b*).

Figure 9. (a) G band for highly ordered pyrolytic graphite (HOPG), MWNT bundles, one isolated semiconducting SWNT and one isolated metallic SWNT. (b) ω_{G} (open symbols) versus ω_{RBM} (bottom axis) and $1/d_t$ (top axis) for several isolated semiconducting SWNTs. Experimental data obtained with $E_{\mathrm{laser}} = 1.58$, 2.41 and 2.54 eV. The $\o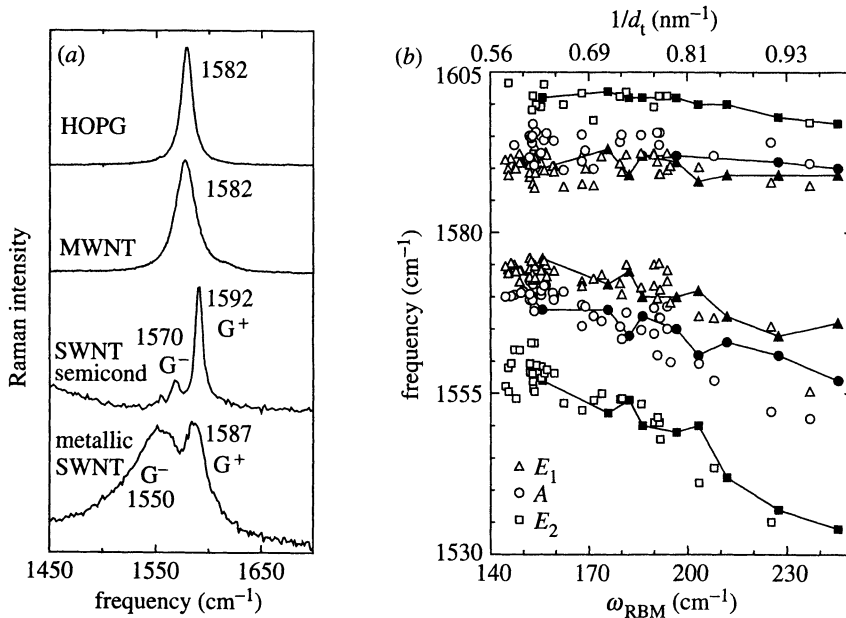mega_{\mathrm{G}}$ are clearly dependent on d_t, but there is no clear evidence for any ω_{G} dependence on E_{laser}. The spectra with $\omega_{\mathrm{RBM}} > 200$ cm^{-1} were obtained with $E_{\mathrm{laser}} = 1.58$ eV. Solid symbols connected by solid lines come from *ab initio* calculations (Dubay *et al.* 2002) downshifted by 18, 12, 12, 7, 7, 11 cm^{-1} from the bottom to the top of these six *ab initio* curves, respectively.

The resonant window for a first-order Raman feature, such as the RBM mode, can be calculated within third-order time dependent perturbation theory,

$$
\left.
\begin{aligned}
I(E_{\mathrm{l}}) &= \sum_{\boldsymbol{k}} |K(\boldsymbol{k})|^2, \\
K(\boldsymbol{k}) &= \frac{M_{\mathrm{opt}}^{\mathrm{abs}}(\boldsymbol{k}) M_{\mathrm{el\text{-}ph}}^{\mathrm{S/AS}}(\boldsymbol{k}) M_{\mathrm{opt}}^{\mathrm{ems}}(\boldsymbol{k})}{[E_{\mathrm{l}} - E(\boldsymbol{k}) - \mathrm{i}\Gamma][E_{\mathrm{l}} \mp \hbar\omega_{\mathrm{ph}} - E(\boldsymbol{k}) - \mathrm{i}\Gamma]},
\end{aligned}
\right\} \tag{3.2}
$$

where $K(\boldsymbol{k})$ is the third-order matrix element; $\boldsymbol{k}$ is the wave vector of the initial electronic state; $M_{\mathrm{opt}}^{\mathrm{abs}}$, $M_{\mathrm{el\text{-}ph}}^{\mathrm{S/AS}}$ and $M_{\mathrm{opt}}^{\mathrm{ems}}$ are, respectively, the transition matrix elements for the optical absorption, electron–phonon interaction for either the Stokes (phonon emission) or anti-Stokes (phonon absorption) processes, and optical emission; E_{l} is the laser excitation energy; ω_{ph} is the zone-centre phonon frequency; $E(\boldsymbol{k}) = E_{\mathrm{c}}(\boldsymbol{k}) - E_{\mathrm{v}}(\boldsymbol{k})$ is the electronic transition energy; Γ is proportional to the inverse lifetime for the scattering process; the '$\mp$' signs correspond to the Stokes (−)/anti-Stokes (+) processes, i.e. phonon emission (−)/absorption (+) (Martin & Falicov 1983).

By using a tunable system and tuning over one electronic transition E_{ii} of a single isolated nanotube, it is possible to determine E_{ii} and Γ. Such an experiment was performed (see figure 8) (Jorio *et al.* 2001b), for an SWNT with $\omega_{\mathrm{RBM}} = 173.6$ cm^{-1},

i.e. $d_t = 248/173.6 = 1.43$ nm. Values for $E_{ii} = 1.655 \pm 0.003$ eV and $\Gamma = 8$ meV were also found from figure 8. Knowing d_t and E_{ii} allowed the assignment of the measured SWNT as the $(18,0)$ metallic SWNT (Jorio *et al.* 2001*b*).

In the upper inset of figure 8*c*, it is shown that the resonance window for the Stokes and anti-Stokes spectra are displaced from each other, due to the $\pm \hbar \omega_{ph}$ factor. This displacement makes it possible to find E_{ii} experimentally without using a tunable system, by just measuring the anti-Stokes/Stokes intensity ratio with a single laser line (Souza Filho *et al.* 2001, 2004). Measurements of the anti-Stokes/Stokes intensity ratio for the RBM feature of many isolated SWNTs on Si/SiO$_2$ substrates show that the simple nearest-neighbour TB model describes the E_{ii} values well for nanotubes with diameters larger than 1.2 nm. These measurements are well described considering $\gamma_0 = 2.89$ eV. The experimental and calculated E_{ii} values start to deviate from each other for smaller diameter SWNTs, with the experimental values of E_{22}^S lying below the TB calculated E_{22}^S for SWNTs with smaller diameters (Souza Filho *et al.* 2004).

The natural line widths for the RBM feature observed for isolated SWNTs on an Si/SiO$_2$ substrate are $\gamma_{RBM} = 3$ cm^{-1}, although larger Γ_{RBM} values are usually observed due to broadening effects (Jorio *et al.* 2002*a*). The broadening has been observed to increase as the SWNT diameter is increased, and $\Gamma_{RBM} > 20$ cm^{-1} values have been observed for $d_t > 2$ nm.

For SWNT bundles, the relation $\omega_{RBM} = A/d_t + B$ applies, where B is an upshift coming from tube–tube interaction, and $A = 234$ cm^{-1} nm and $B = 10$ cm^{-1} have been found for SWNT bundles (Kuzmany *et al.* 2001; Milnera *et al.* 2000). For the usual diameter range $1 < d_t < 2$ nm, the two sets of parameters (for isolated (Jorio *et al.* 2001*a*) and bundled (Kuzmany *et al.* 2001; Milnera *et al.* 2000) SWNTs) give similar d_t for a given ω_{RBM}, differing considerably only for $d_t < 1$ nm and $d_t > 2$ nm. However, for $d_t < 1$ nm, the simple $\omega_{RBM} = A/d_t + B$ relation is not expected to hold due to nanotube lattice distortions leading to a chirality dependence of ω_{RBM} (Kürti *et al.* 2003). For large-diameter tubes ($d_t > 2$ nm), the intensity of the RBM feature is weak and is hardly observable, probably due to a weaker quantum confinement and broadening effect.

In SWNT bundles, a single Raman measurement gives an idea of the special nanotubes that are in resonance with that laser line, but does not give a complete characterization of the diameter distribution of the sample. However, by taking Raman spectra using many laser lines, a good characterization of the diameter distribution in the sample can be obtained (Milnera *et al.* 2000). A careful analysis of figure 4, considering the E_{laser} line to be used, should be made to correctly understand the RBM information that can be obtained from the Raman spectra from an actual SWNT sample.

(*c*) *The G band*

The G band can also be used to characterize SWNT samples. Figure 9*a* shows the G band for graphite, MWNT bundles, one isolated semiconducting SWNT and one isolated metallic SWNT. Figure 9*b* shows that the G band frequency also depends on the SWNT diameter.

The G band accounts for six Raman allowed modes appearing in the frequency region 1500–1600 cm^{-1}. The G comes from graphite, since this band is related to the

Table 1. *Diameter dependence of some features observed in the Raman spectra of isolated SWNTs*

(Here ω_0 denotes the mode frequency associated with 2D graphite, whose value depends on the laser excitation energy, if the mode is associated with a double-resonance process. Frequencies are in units of cm^{-1} and the tube diameter d_t is in units of nm. The coefficients for the D, M, and G$'$ bands were obtained by using data measured with $E_{laser} = 2.41$ eV. $\bar{\omega} = \omega_0 + \beta/\bar{d}_t^n$.)

mode	frequency ω_0	exponent n	diameter coefficient β
RBM	0	1	248[a]
D	ω_D^0	1	-16.5[b]
G$^+$	1591	0	0
G$^-$	1591	2	$(-45.7; -79.5)$[c]
M$^+$	ω_{M+}^0	1	-18.0[d]
M$^-$	ω_{M-}^0	1	-16.7[d]
G$'$	$\omega_{G'}^0$	1	-35.4[b]

[a]Jorio *et al.* (2001a).
[b]This value was obtained using $E_{laser} = 2.41$ eV. By using the spectra obtained with 1.58 eV, a $\beta = -18.9$ cm^{-1} nm value was obtained (Souza Filho *et al.* 2003).
[c]The coefficient β for the G$^-$ component is, respectively, -45.7 and -79.5 cm^{-1} nm^2 for semiconducting and metallic SWNTs. The 1.58, 2.41 and 2.54 eV laser lines were used to obtain the G band experimental results used in the fitting procedure (Jorio *et al.* 2002d).
[d]Brar *et al.* (2002).

graphite tangential E_{2g_2} Raman active mode, where the two atoms in the graphene unit cell are vibrating tangentially one against the other. The Raman allowed tangential mode in graphite is observed at 1582 cm^{-1} (see figure 9a). Unlike graphite, the tangential G mode in SWNTs gives rise to a multi-peak feature because of the symmetry breaking of the tangential vibration when the graphene sheet is rolled to make a cylindrically shaped tube, and because of quantum confinement of the phonon wave vector along the nanotube circumference (see figure 6).

The A, E_1 and E_2 symmetry modes are Raman allowed, and each of them can exhibit carbon atom vibrations along the nanotube axis or along the circumferential direction, thus resulting in six Raman active modes (see figure 6). This feature can be used to characterize d_t (although it is less accurate than the RBM), to differentiate metallic SWNTs from semiconducting SWNTs, and then to obtain other important information related to polarization analysis of Raman spectra, which is the subject of the next subsection.

Figure 9b shows the diameter dependence of the G mode frequencies (ω_G), for the six Raman allowed G band modes from semiconducting SWNTs. The upper frequency A, E_1 and E_2 modes, or G$^+$ group, associated with atomic vibrations along the nanotube axis, is practically independent of tube diameter. The lower frequency A, E_1 and E_2 modes, or G$^-$ group, associated with vibrations along the nanotube circumference, decreases with decreasing d_t, and this decrease becomes larger as the curvature of the SWNT increases (Jorio *et al.* 2003).

For a simpler picture, the G band profile can be fit by using only two peaks, one for the G$^+$ feature and one for the G$^-$ feature, for both metallic and semiconducting

SWNTs (Jorio *et al.* 2002*d*). The splitting

$$\Delta\omega_{\mathrm{G}} = \omega_{\mathrm{G}+} - \omega_{\mathrm{G}-}$$

can then be used for diameter characterization (see table 1). If isolated SWNTs are measured, the value of $\Delta\omega_{\mathrm{G}}$ refers to the particular tube in question, but if SWNT bundles are measured, the $\Delta\omega_{\mathrm{G}}$ will be roughly related to the maximum in the Gaussian diameter distribution of the sample, but does not accurately reflect the diameter dependence of $\omega_{\mathrm{G}-}$. Note from the β parameter in table 1 that the downshift on $\omega_{\mathrm{G}-}$ is much larger for metallic SWNTs than for semiconducting SWNTs.

The difference between the G band line shape for semiconducting and metallic SWNTs is evident in the line shape of the G^- feature (see figures 1 and 9*a*), which is broadened for metallic SWNTs in comparison with the Lorentzian line shape for semiconducting tubes, and this broadening is related to the presence of free electrons in nanotubes with metallic character (Brown *et al.* 2001; Pimenta *et al.* 1998). This broadened G^- feature is usually fitted using a Breit–Wigner–Fano (BWF) line that accounts for the coupling of a discrete phonon with a continuum related to the conduction electrons (Brown *et al.* 2001; Jiang *et al.* 2002). This BWF line is observed in many graphite-like materials with metallic character, such as n-doped graphite intercalation compounds (GIC) (Dresselhaus & Dresselhaus 1981, 2002), n-doped fullerenes, as well as metallic SWNTs.

Considering the (E_{ii} versus d_{t}) plot in figure 4, for a given E_{laser} line, one can predict the diameter range where semiconducting-like G^- band line shapes will be observed and the diameter range for which the metallic-like G^- band line shapes should be observed (Pimenta *et al.* 1998). Observation of a metallic-like G^- band when a semiconducting line shape should be observed indicates the presence of charged impurities (Rao *et al.* 1997*b*). Electro-chemical doping also changes the G band characteristics (as well as frequencies) (Corio *et al.* 2003).

The line widths $\Gamma_{\mathrm{G}+}$ for the G peaks from isolated SWNTs are usually around 5–15 cm^{-1}, and the same range of line widths for $\Gamma_{\mathrm{G}-}$ are found for semiconducting isolated SWNTs (Jorio *et al.* 2002*a*). For semiconducting SWNTs in bundles, the line widths are related to the diameter distribution, and therefore the broadening principally occurs for $\Gamma_{\mathrm{G}-}$. For metallic SWNTs, the broadening is minor for $\Gamma_{\mathrm{G}+}$, while for $\Gamma_{\mathrm{G}-}$ a significant broadening occurs, and it is found that the line width for the BWF line is strongly dependent on tube diameter. For isolated tubes with $d_{\mathrm{t}} > 2$ nm, $\Gamma_{\mathrm{G}-}$ is similar to semiconducting SWNTs, and the G^- feature mostly looks like a normal Lorentzian, reflecting the small magnitude of the BWF effect. The BWF effect increases as the tube diameter decreases, causing the G^- feature to become more asymmetric and broad. Values of $\Gamma_{\mathrm{G}-} > 70$ cm^{-1} have been observed for isolated metallic SWNTs (Jorio *et al.* 2002*a*).

(*d*) *Polarization analysis*

Polarization of the incident and scattered light is not an important issue for a sample of misaligned carbon nanotubes, but polarization effects are very important for the Raman response of a sample of aligned carbon nanotubes (either aligned bundles or a single straight carbon nanotube). There is a general and simple polarization behaviour that one should have in mind when acquiring the Raman spectra from a sample of aligned carbon nanotubes. Carbon nanotubes behave as antennas, with the
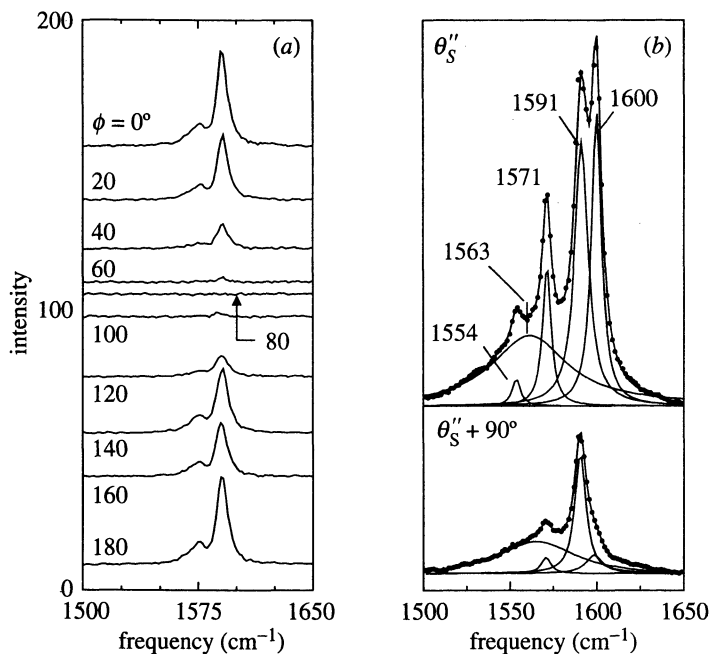
Figure 10. (a) Polarization dependence of the G band from one isolated semiconducting SWNT sitting on an Si/SiO₂ substrate (Jorio et al. 2002b) with incident and scattered light polarized parallel to each other. $\phi = 0°$ stands for the incident light polarized along the nanotube axis. (b) Polarization scattering geometry dependence for the G band from one isolated SWNTs in resonance with $E_{\text{laser}} = 2.41$ eV. The Lorentzian peak frequencies are in cm^{-1}. θ_S'' denotes the initial angle between the light polarization and the SWNT axis direction, not known a priori. From the relative intensities, and the polarization behaviour of the G band modes, $\theta_S'' \sim 90°$ was assigned (Jorio et al. 2003), and the mode symmetries are E₂ for the 1554 and 1600 cm^{-1} peaks and A for the 1571 and 1591 cm^{-1} peaks. The broad feature at 1563 cm^{-1} is assigned as a disorder-induced feature, as discussed in § 4 b (ii).

absorption/emission of light being highly suppressed for light polarized perpendicular to the nanotube axis. Therefore, if one wants to measure Raman spectra from a sample of aligned carbon nanotubes, the largest Raman intensity will generally be observed for light polarized along the tube axes, and almost no signal will be observed for cross-polarized light (Duesberg et al. 2000; Hwang et al. 2001; Jorio et al. 2002b), as shown in figure 10a.

This antenna effect is expected by symmetry selection rules. When acquiring the polarized spectra from a single SWNT with a fixed laser energy, it is not possible to observe Raman signals from both parallel and perpendicular polarization, since the resonance energies for the polarized light in these polarization directions are different from each other (see § 3 a). Furthermore, the depolarization effect, which screens optical absorption and emission of cross-polarized light (Ajiki & Ando 1994; Marinopoulos et al. 2003) must be considered.

However, the most interesting results coming from polarization analysis are related to the symmetry selection rules for the different phonon/electron symmetries (Jorio et al. 2000, 2002b; Rao et al. 2000). Polarization analysis of the Raman spectra from both isolated SWNTs and bundles of SWNTs show that it is possible to observe the

predictions from group theory. This result is clear when observing the appearance and disappearance of the E_2 symmetry modes, as shown in figure 10b. According to symmetry selection rules (see equation (3.1)), the A symmetry modes can be observed for both (ZZ) and (XX) scattering geometries, while E_2 symmetry modes can only be observed for the (XX) scattering geometry (see also the table in figure 6). The clear observation of strong E_2 modes in figure 10b indicates that a resonance Raman signal is obtained with both the absorption and emission of light for light crossed polarized with respect to the nanotube axis, in disagreement with the general polarization result expected due to the antenna effect. Observation of cross-polarized light is important for showing that electronic transitions between neighbouring cutting lines $(E_\mu \leftrightarrow E_{\mu\pm1})$ can indeed be observed. Study of these transitions across two different cutting lines is expected to make it possible to assign the valence/conduction bands asymmetry around the Fermi level using optical transitions (Jorio *et al.* 2003). Careful experiments using a tunable laser on a single SWNT in resonance with an $(E_\mu \leftrightarrow E_{\mu\pm1})$ transition and a polarization analysis of the resulting spectra will be necessary to extract the important physics related to the Raman spectra using cross-polarized light.

4. Double-resonance Raman spectra

The double-resonance Raman scattering process involves the following steps: light absorption, scattering by a phonon (symmetry E_μ and momentum q), scattering by another phonon $(E_{\mu',q'})$ (combination mode) or by a defect (disorder-induced mode), and finally light emission. For the ZZ scattering geometry, selection rules for combination modes requires $\mu = \mu'$ and $q' = -q$, for angular and linear momentum conservation, respectively. In the case of disorder-induced modes, defects can mix electronic states and there is no symmetry requirement.

Such a process is usually much less intense than first-order single-resonance Raman scattering, because it exhibits an extra scattering process. However, when one of the internal scattering processes (by a phonon or by a defect) connects two real electronic states, this process can become comparable in intensity with the first-order single-resonance Raman process, and therefore Raman peaks associated with a double-resonance process can also be observed. In the double-resonance process, resonance with either the incident or scattered light plus resonance with the internal (intermediate) scattering event occurs.

More details about the double-resonance physics related to graphite can be found in Thomsen *et al.* (2004). In the case of carbon nanotubes, however, the strong confinement of electrons and phonons into VHSs makes the usual dispersive behaviour of the double-resonance features to be discrete, with the Raman spectra being observable only for specific phonons connecting specific electronic states. Energy and momentum conservation requirements for the double-resonance process, together with electron and phonon confinement into 1D VHSs, then make it possible to address specific points in the interior of the Brillouin zone. For this reason, the combination modes or disorder-induced features turn out to give very interesting and accurate information about both the vibrational and electronic structure of SWNTs. Such information is not available by analysis of the first-order single-resonance features, and this is mostly due to the sensitivity of the double-resonance process to the chirality of SWNTs.

(a) Combination modes

The observation of sharp peaks associated with combination modes is common in the Raman spectra from molecules, but is unusual in the Raman spectra from solids, because the continuum of phonon states in bulk materials results in higher-order (combination mode) Raman scattering with very broad, poorly resolved spectral features. However, phonon confinement in SWNTs generates VHSs in the phonon DOS, and interesting effects associated with sharp combination mode features are observed through the double-resonance process.

The phonon dispersion in SWNTs is rich and several different harmonics and combination modes have been observed in SWNTs (Brown *et al.* 2000; Dresselhaus & Eklund 2000). They can usually be related to a combination of specific branches from the phonon dispersion in graphite, such as $G' = 2D$ (Pimenta *et al.* 2000), iTO + LA and 2oTO (Brar *et al.* 2002), etc. (see figure 1). Combination modes are interesting for nanotube characterization, first because they give information about many phonon branches not active in first-order Raman scattering, and second because they exhibit chirality-dependent frequencies. This chirality dependence of the peak frequencies for the weak spectral features can be understood, considering that they usually come from phonons associated with interior points in the anisotropic 2D Brillouin zone. Different (n, m) nanotubes imply different folding of the 2D phonon dispersion relations. For a fixed phonon wave vector magnitude $|q|$ measured from a high symmetry point (e.g. the K point), the phonon frequencies are different for different phonon propagation directions. During the folding process, this property results in having phonon frequencies for nanotubes with fixed d_t, depending on the chiral angle θ.

The so-called G' band is a Raman feature observed in highly ordered pyrolytic graphite (HOPG), and it has been very informative about SWNT vibrational and electronic structure. This feature is the overtone of the well-known D band (see next section) and appears in SWNTs around $2700\,\mathrm{cm}^{-1}$, exhibiting a strong frequency dispersive behaviour as E_{laser} is varied, $\Delta\omega_{G'}/\Delta E_{\mathrm{laser}} = 106\,\mathrm{cm}^{-1}\,\mathrm{eV}^{-1}$ (Pimenta *et al.* 2000).

Unusual double peak G' features depending on (n, m) give detailed information about the position of the electronic VHSs. For *metallic* SWNTs, the VHSs are known to split in energy due to the trigonal warping effect, distorting the equi-energy contours around the K point in the graphite Brillouin zone. This splitting is observed in the G' feature, and measurement of the splitting $\Delta\omega_{G'}$ versus chiral angle θ gives the chirality dependence of the energy splitting between the two VHSs in metallic SWNTs (Souza Filho *et al.* 2002a). Unusual double peak G' features depending on (n, m) are also observed for a few semiconducting SWNTs exhibiting VHSs spaced by the G' energy (Souza Filho *et al.* 2002b). In this case, resonance with both incident and scattered light can be achieved, each process giving a different $\omega_{G'}$. Measurements of $\Delta\omega_{G'}$ for semiconducting SWNTs therefore give information at once about the energy separation between two electronic VHSs (e.g. $E_{44}^S - E_{33}^S$) for one isolated SWNT.

Also interesting is the intermediate frequency mode (IFM) spectral region, appearing between the RBM and the D/G bands (Fantini *et al.* 2004). Figure 11a plots the dependence on the excitation laser energy E_{laser} of the IFM frequencies ω_{IFM}. The
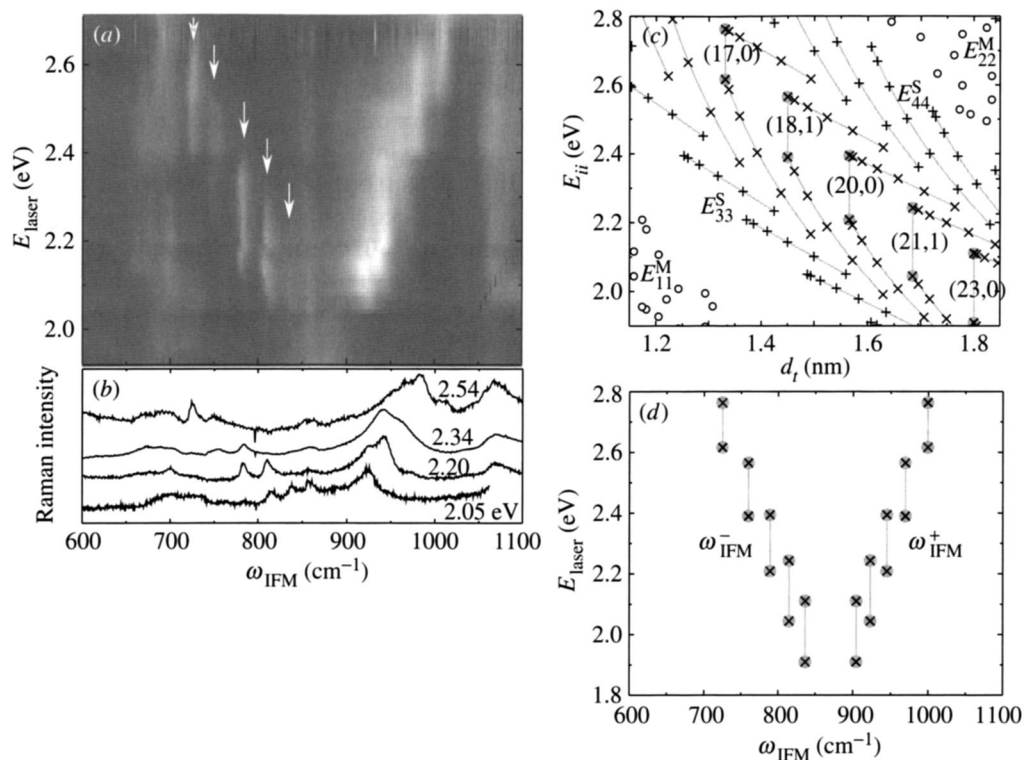
Figure 11. (*a*) Two-dimensional plot for the E_{laser} dependence for frequencies of the features in the Raman spectra of SWNT bundles in the intermediate frequency mode (IFM) range. The light areas indicate high Raman intensity. Arrows point to five well-defined ω_{IFM}^{-} features. (*b*) Raman spectra with $E_{\text{laser}} = 2.05$, 2.20, 2.34, and 2.54 eV. (*c*) VHS E_{ii} transition energies (from the TB model (Dresselhaus *et al.* 2001) with $\gamma_0 = 2.9$ eV and $a_{\text{C-C}} = 0.142$ nm) as a function of d_{t}. The symbols '×', '+' and 'o' stand for semiconducting type-1, type-2 and metallic SWNTs, respectively. Grey curves connect E_{ii}^{S} for SWNTs with $2n + m$ constant. Vertical grey lines connect E_{33}^{S} and E_{44}^{S} for the (n, m) assigned SWNTs. (*d*) Theoretical prediction for the ω_{IFM}^{+} and ω_{IFM}^{-} shown in (*a*). Considering only the E_{33}^{S} and E_{44}^{S} VHSs for the SWNTs assigned in (*c*), the plot in (*d*) is constructed by considering $E_{\text{laser}} = E_{ii}$ and $\omega_{\text{IFM}}^{\pm} = \omega_0^{\pm} + v_{\mathcal{A}}^{\pm}(6/d_{\text{t}})$ (see text).

light areas in figure 11*a* indicate strong Raman intensities. The IFM Raman spectra obtained with $E_{\text{laser}} = 2.05$ eV (red), 2.20 eV (yellow), 2.34 eV (green) and 2.54 eV (blue) are shown in figure 11*b* as examples of the different IFM Raman spectra that are observed. These features are assigned as a combination of an optical phonon with a highly dispersive acoustic-like phonon ($\omega_{\mathcal{O}} \pm \omega_{\mathcal{A}}$), thus forming the 'V' shape structure observed in the centre of figure 11*a*.

Figure 11*a* shows that the $\omega_{\mathcal{O}} \pm \omega_{\mathcal{A}}$ Raman process is effective only for special SWNTs, named semiconducting type-1 nanotubes (for which $\text{mod}(2n + m, 3) = 1$) with $\theta \to 0$, because the double-resonance Raman scattering in SWNTs is extremely selective when considering the confinement of electrons and phonons into VHSs. Only specially selected (n, m) SWNTs can have two electronic states at electronic VHSs (see figure 11*c*) connected by special phonons with frequencies at phonon VHSs, as explained further below.

Figure 11c shows the E_{ii} transition energies as a function of SWNT diameter for the energy range of lasers used in the experiment and shown in figure 11a, and for the d_t range present in the sample. The laser energies are chosen to be near two close-lying *electronic* VHSs, namely E_{33}^S and E_{44}^S, that can only be connected resonantly by E_3 symmetry phonons. Figure 11c can be directly related to the experimental results shown in figure 11a. The Y-axis energy ranges can be related to electronic VHSs by $E_{\text{laser}} = E_{ii}$ for resonance conditions. The X-axis d_t can be transformed into ω_{IFM} by the relation $\omega_{\text{IFM}}^{\pm} = \omega_{\mathcal{O}}^{\pm} + v_{\mathcal{A}}^{\pm} q_{\perp}$, while $q_{\perp} = 6/d_t$ for E_3 symmetry phonons which produce VHSs in the phonon density of states. This transformation is applied only for the E_{33}^S and E_{44}^S VHSs for the specific SWNTs assigned in figure 11c, and the result is shown in figure 11d, where the fitting parameters are $\omega_{\mathcal{O}}^{+} = 540$ cm^{-1} and $\omega_{\mathcal{O}}^{-} = 1195$ cm^{-1}, while $v_{\mathcal{A}} = 2 \times 10^4$ m s^{-1} is the sound velocity in graphite. The similarity between figure 11d and the 'V'-picture observed in figure 11a clearly shows that the step-like dispersive IFMs come from these specific (n, m) SWNTs in figure 11c having $\theta \to 0$.

(b) Disorder-induced features

In the presence of a defect, double resonance can occur with only one phonon, and the defect will mix electronic states with different wave vectors, k, but without symmetry or momentum conservation requirements. Therefore, any phonon within the SWNT Brillouin zone can be observed in a first-order Raman scattering process. As discussed for combination modes, the disorder-induced bands give information about many phonon branches not active in first-order Raman scattering from a highly ordered sample, and the disorder-induced features exhibit chirality-dependent frequencies.

(i) Disorder-induced D band

The most studied disorder-induced feature in SWNTs and other carbon-based materials is the so-called D band (D from 'disorder'), which is related to the high-energy optical phonons in the vicinity of the K point in graphite. The largest interest in studying these phonon features is for defect characterization. Until now no systematic study has been carried out to correlate the presence of the D band with specific defect types (such as hetero-atoms, vacancies, heptagon–pentagon pairs, kinks, or even the presence of impurities, etc.). However, relevant information has been obtained.

From a large number of Raman spectra from isolated SWNTs grown by CVD on an Si/SiO$_2$ substrate (over 100 signals from physically different tubes), *ca.* 50% exhibit observable D band signals with weak intensity (usually 100 times smaller than the G band). The following two characteristics differentiate the D band in carbon nanotubes from the D band in defective graphite.

Small line widths. From the observation of a large number of D bands from isolated SWNTs, Γ_D HWHM values from 40 cm^{-1} down to 7 cm^{-1} have been observed (Jorio *et al.* 2002a), reflecting electron and phonon confinement. Lorentzian lines were used to fit the D band features as an approximation for interpreting their behaviour, although it is known that the disorder-induced D band appears in the Raman spectra

of graphite-like materials through a double-resonance process (Saito *et al.* 2002; Thomsen & Reich 2000), where inhomogeneous broadening occurs.

Complex frequency behaviour. The D band frequency ω_D depends directly on the nanotube diameter d_t and also on the magnitude of the wave vector for the quantized state k_{ii}, where the VHSs in the density of states occur (Souza Filho *et al.* 2003). These two effects are manifested in the diameter dependence of the D band frequency, which satisfies the

$$\omega_D = \omega_D^0 + \frac{C}{d_t}$$

functional form, but the C is negative (positive) for the spring-constant (double-resonance)-dependent process, thereby indicating that the spring constant softens (downshifts) and the double-resonance stiffens (upshifts) the D band frequencies. In the case of the spring constant effect, ω_D^0 is the frequency observed in 2D graphite (see table 1).

Besides the d_t dependence of ω_D, the D band was shown to exhibit a $\Delta\omega_D = 24\ \mathrm{cm}^{-1}$ frequency difference between armchair and zigzag SWNTs when excited with $E_{\mathrm{laser}} = 2.41\ \mathrm{eV}$ (Samsonidze *et al.* 2003*b*). Furthermore, this D band feature was observed to exhibit an interesting line shape dependence on the resonance condition (including for SWNT bundles (Pimenta *et al.* 2000; Zólyomi *et al.* 2003)), giving detailed information about the position of the electronic VHSs from isolated SWNTs, as discussed for its overtone G′ band (see the previous section).

(ii) *Disorder-induced G band*

Besides the D band, any Raman branch can give rise to a defect-induced feature, and Raman data from SWNTs were used to probe the phonon dispersion in graphite (Saito *et al.* 2002). Maultzsch *et al.* (2002) studied the double-resonance process applied to the G band phonon branches. Although six G band modes are predicted in first-order Raman scattering, Maultzsch *et al.* observed an E_{laser} dependence of the G band frequencies in their Raman spectra, and interpreted dispersive behaviour as providing experimental evidence for double-resonance scattering.

As for the D band, the observation of G band double-resonance features is related to defects in the sample. In a defect-free aligned SWNT, the G band first-order single-resonance process, as discussed in § 3 *c*, is the only feature observed in the Raman spectra. However, in a highly defective and disordered SWNT sample, the double-resonance G band components can also be observed, exhibiting an intensity similar to that of first-order single-resonance features, as shown in figure 12 (Souza *et al.* 2003).

Resonance Raman spectra of the G band from a fibre of an aligned SWNT bundle sample (Hwang *et al.* 2001) was acquired in the (ZZ) polarization scattering geometry. From this sample, G band spectra from defect-free aligned SWNTs are observed (see spectra in figure 12*a*, obtained at location '1' shown in the inset) (Souza *et al.* 2003). Two 'A' symmetry modes are then observed, in agreement with symmetry selection rules for first-order single-resonance Raman scattering. Raman spectra were also taken at the edge of the same fibre (location '2' in the inset to figure 12*a*), where misalignment, edge defects and impurities are abundant, and a typical spectrum observed in this case is shown in figure 12*b*. The spectrum at the
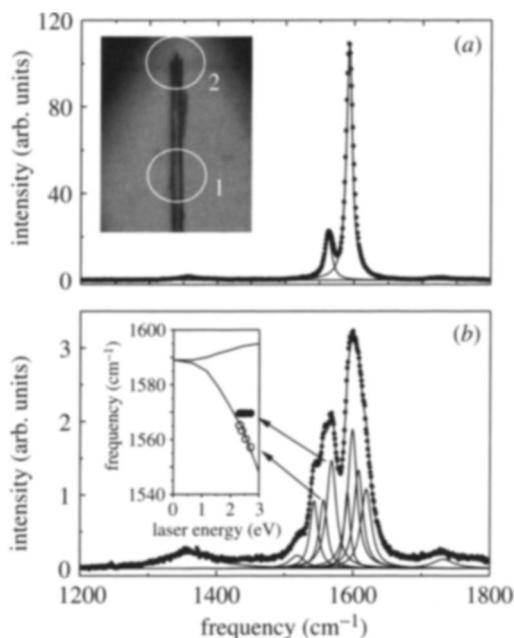
Figure 12. (*a*) Resonance Raman spectrum taken in the (ZZ) polarization scattering geometry (location '1') of the G band from a fibre of an aligned SWNT bundle sample. The inset shows two positions on the fibre sample (optical image). (*b*) G band Raman spectrum taken at the edge of the fibre (location '2') (Souza *et al.* 2003). The inset shows the E_{laser} dependence of the two peaks indicated by arrows, one showing a strong E_{laser} dependence, and the other showing no E_{laser} dependence. The solid lines are predictions for the E_{laser} dependence of the G band double-resonance features in graphite (Saito *et al.* 2002).

edge shows many features (more than the six predicted for first-order Raman scattering), and some of them are dispersive. The different features observed in figure 12*b* were assigned to either single or double-resonance processes. For example, the inset to figure 12*b* shows that the feature observed at *ca.* 1560 cm^{-1} (open circles) is dispersive, while the feature observed at *ca.* 1570 cm^{-1} (filled circles) is not. These two peaks were therefore assigned as double-resonance and single-resonance E_1 symmetry phonons, respectively (Souza *et al.* 2003). Note that the intensity for the Raman spectrum in the highly defective and misaligned sample is about two orders of magnitude lower than the spectrum in the defect-free aligned SWNT sample. However, in the defective and misaligned sample, defect-induced double-resonance features are observed with intensities comparable to the first-order single-resonance features for that sample.

5. Spectra from other carbon nanotube systems

The results discussed above address the most usual SWNTs that have been produced and studied ($1 < d_t < 3$ nm). However, it is also interesting to comment about Raman spectra from the SWNTs with $d_t = 0.4$ nm inside zeolite templates, and Raman spectra from MWNTs.

Intensive effort has been devoted to the smallest-diameter SWNTs, with $d_t = 0.4$ nm, grown inside zeolite templates (Wang *et al.* 2000). Raman spectroscopy has

been used to characterize these samples, showing interesting and very rich spectra (Sun *et al.* 1999). Their RBM features are consistent with the assigned diameters for the three possible (n, m) SWNTs that could be grown within the tiny pores of the zeolite template, namely $(3, 3)$, $(4, 2)$ and $(5, 0)$. The G band appears to be complex, showing a very large $(\omega_{G+} - \omega_{G-})$ splitting. Furthermore, several other IFM features are observed, and they are assigned to the SWNT phonon density of states (Jorio *et al.* 2002*c*).

In the case of MWNTs, because of the typical large diameter of the outer tubes, most of the characteristic differences that distinguish the Raman spectra in carbon nanotubes from those for graphite are not so evident. The RBM from large-diameter tubes (above 3 nm in diameter) is usually too weak to be observable. Whereas the $(\omega_{G+} - \omega_{G-})$ splitting is large for small-diameter tubes (see § 3 *c*), this double-peak G band splitting for large-diameter MWNTs is both small in frequency and smeared out because of the diameter distribution of the constituents of an MWNT. Therefore, the G band feature predominantly exhibits a weakly asymmetric characteristic, with a peak appearing close to the graphite frequency $1582 \, \text{cm}^{-1}$ (see figure 9) (Rao *et al.* 2000). These properties make it more difficult to differentiate the Raman signal of MWNTs from that of graphite and other sp^2 carbons. The Raman features associated with the small-diameter inner tubes can sometimes be observed when a good resonance condition is established (Benoit *et al.* 2002; Zhao *et al.* 2002), but obtaining a good resonance condition with the innermost shell is not a common result.

6. Using SWNTs to learn about graphite

As discussed in § 4, combination modes and disorder-induced features give information about many phonon branches that are not Raman active in first-order Raman scattering, with these disorder-induced features exhibiting chirality-dependent frequencies. These properties can be used, as an inverse problem in applied mathematics, to get information one could not otherwise obtain from the Raman spectra of graphite. The D band feature gives a clear example of this approach, as illustrated below.

In graphite, double-resonance energy and momentum conservation requirements select the magnitude of the phonon momentum $|q|$ participating in the scattering process. Therefore, a large number of phonons satisfy the double-resonance energy and momentum conservation requirements for a given E_{laser} (Cançado *et al.* 2002), and a broad double-resonance Raman feature is observed. However, the quantum confinement of electrons in the 1D structure of SWNTs allows one to address specific phonon directions in the 2D reciprocal space of graphite because of the relation $q \simeq -2k$ between the phonon (q) and the electron (k) wave vectors in the double-resonance process. The different (n, m) nanotubes imply different folding of the 2D phonon dispersion relations. Thus, not only is the magnitude of the phonon momentum $|q|$ selected, but also the q-direction is selected by the SWNT chiral angle θ.

The D band for SWNTs is shown to exhibit a $\Delta\omega_D = 24 \, \text{cm}^{-1}$ frequency difference between armchair and zigzag SWNTs when excited with $E_{\text{laser}} = 2.41 \, \text{eV}$ (Samsonidze *et al.* 2003*b*). For a fixed phonon wave vector magnitude $|q|$ measured from a high symmetry point (e.g. the K point), the phonon frequencies are different for different phonon propagation directions, and the trigonal warping effect is

observed in the phonon equi-energies around the K point. Measuring the chirality dependence of ω_D is equivalent to a measurement of the trigonal warping effect of phonons in graphite around the K point. Such a measurement would be never possible in the Raman spectra of graphite, where only an average over the 2D reciprocal space can be obtained.

7. Summary

Raman spectroscopy of nanotubes can be performed at room temperature, under ambient pressure, and at the single-nanotube level in nanodevices (Jorio *et al.* 2002*e*). The large amount of information that becomes available from Raman spectroscopy at the isolated SWNT level has provided many new results for the development of more complete theoretical models describing nanotube physics. The unique optical properties observed in SWNTs are related to the 1D confinement of electronic states resulting in VHSs, and this property is not restricted to SWNTs, but, in principle, occurs in any 1D material of sufficiently small size. The features originating from internal resonance processes (resonant electron–phonon scattering) have also provided a large amount of information about electrons and phonons within the interior of the Brillouin zone, and this new physics can probably be extended to any semi-conducting material. Therefore, the capability of this technique, stemming from the fact that it uses light as a non-invasive probe, establishes Raman spectroscopy as an important technique for studying nanomaterials.

References

Ajiki, H. & Ando, T. 1994 *Physica* B **201**, 349.

Alon, O. E. 2001 *Phys. Rev.* B **63**, 201403(R).

Benoit, J. M., Buisson, J. P., Chauvet, O., Godon, C. & Lefrant, S. 2002 *Phys. Rev.* B **66**, 073417.

Berber, S., Kwon, Y.-K. & Tománek, D. 2000 *Phys. Rev. Lett.* **84**, 4613.

Bethune, D. S., Kiang, C. H., de Vries, M. S., Gorman, G., Savoy, R., Vazquez, J. & Beyers, R. 1993 *Nature* **363**, 605.

Brar, V. W., Samsonidze, Ge. G., Dresselhaus, G., Dresselhaus, M. S., Saito, R., Swan, A. K., Ünlü, M. S., Goldberg, B. B., Souza Filho, A. G. & Jorio, A. 2002 *Phys. Rev.* B **66**, 155418.

Brown, S. D. M., Jorio, A., Corio, P., Dresselhaus, M. S., Dresselhaus, G., Saito, R. & Kneipp, K. 2000 *Phys. Rev.* B **61**, 7734–7742.

Brown, S. D. M., Jorio, A., Corio, P., Dresselhaus, M. S., Dresselhaus, G., Saito, R. & Kneipp, K. 2001 *Phys. Rev.* B **63**, 155414.

Cançado, L. G. *et al.* 2002 *Phys. Rev.* B **66**, 035415.

Corio, P. *et al.* 2003 *Chem. Phys. Lett.* **370**, 675–682.

Damnjanović, M., Milosević, I., Vuković, T. & Srendanović, R. 1999 *Phys. Rev.* B **60**, 2728.

Dresselhaus, M. S. & Dresselhaus, G. 1981 *Adv. Phys.* **30**, 139–326.

Dresselhaus, M. S. & Dresselhaus, G. 2002 *Adv. Phys.* **50**, 1–186.

Dresselhaus, M. S. & Eklund, P. C. 2000 *Adv. Phys.* **49**, 705–814.

Dresselhaus, M. S., Dresselhaus, G. & Avouris, Ph. 2001 *Carbon nanotubes: synthesis, structure, properties and applications.* Springer.

Dubay, O. & Kresse, G. 2003 *Phys. Rev.* B **67**, 035401.

Dubay, O., Kresse, G. & Kuzmany, H. 2002 *Phys. Rev. Lett.* **88**, 235506.

Duesberg, G. S., Loa, I., Burghard, M., Syassen, K. & Roth, S. 2000 *Phys. Rev. Lett.* **85**, 5436–5439.

Fantini, C. (and 10 others) 2004 *Phys. Rev. Lett.* **93**, 087401.

Grüneis, A., Saito, R., Kimura, T., Cançado, L. G., Pimenta, M. A., Jorio, A., Souza Filho, A. G., Dresselhaus, G. & Dresselhaus, M. S. 2002 *Phys. Rev.* B **65**, 155405.

Hwang, J. *et al.* 2000 *Phys. Rev.* B **62**, R13301.

Iijima, S. 1991 *Nature* **354**, 56–58.

Iijima, S. & Ichihashi, T. 1993 *Nature* **363**, 603.

Jiang, C., Kempa, K., Zhao, J., Schlecht, U., Kolb, U., Basché, T., Burghard, M. & Mews, A. 2002 *Phys. Rev.* B **66**, 161404.

Jishi, R. A., Venkataraman, L., Dresselhaus, M. S. & Dresselhaus, G.1993 *Chem. Phys. Lett.* **209**, 77–82.

Jorio, A., Dresselhaus, G., Dresselhaus, M. S., Souza, M., Dantas, M. S. S., Pimenta, M. A., Rao, A. M., Saito, R., Liu, C. & Cheng, H. M. 2000 *Phys. Rev. Lett.* **85**, 2617–2620.

Jorio, A., Saito, R., Hafner, J. H., Lieber, C. M., Hunter, M., T. McClure, Dresselhaus, G. & Dresselhaus, M. S., 2001a *Phys. Rev. Lett.* **86**, 1118–1121.

Jorio, A., Souza Filho, A. G., Dresselhaus, G., Dresselhaus, M. S., Saito, R., Hafner, J. H., Lieber, C. M., Matinaga, F. M., Dantas, M. S. S. & Pimenta, M. A. 2001b *Phys. Rev.* B **63**, 245416.

Jorio, A. (and 12 others) 2002a *Phys. Rev.* B **66**, 115411.

Jorio, A. (and 11 others) 2002b *Phys. Rev.* B **65**, R121402.

Jorio, A. (and 11 others) 2002c *Chem. Phys. Lett.* **351**, 27–34.

Jorio, A. (and 10 others) 2002d *Phys. Rev.* B **65**, 155412.

Jorio,-A. *et al.* 2002e *Brazil. J. Phys.* **32**, 921–924.

Jorio, A., Samsonidze, Ge. G., Dresselhaus, G., Pimenta, M. A., Dresselhaus, M. S., Swan, A. K., Ünlü, M. S., Goldberg, B. B. & Saito, R. 2003 *Phys. Rev. Lett.* **90**, 107403.

Journet, C., Maser, W. K., Bernier, P., Loiseau, A., Lamy de la Chapelle, M., Lefrant, S., Deniard, P., Lee, R.& Fischer, J. E.1997 *Nature* **388**, 756–758.

Kataura, H. (and 11 others) 1999 *Synth. Metals* **103**, 2555.

Kim, P., Shi, L., Majumdar, A. & McEuen, P. L. 2001 *Phys. Rev. Lett.* **87**, 215502.

Kürti, J. *et al.* 2004 *Carbon* **42**, 971–978.

Kuzmany, H., Plank, W., Hulman, M., Kramberger, Ch., Grüneis, A., Pichler, Th., Peterlik, H., Kataura, H. & Achiba, Y. 2001 *Eur. Phys. J.* B **22**, 307–320.

Marinopoulos, A. G., Reining, L., Rubio, A. & Vast, N. 2003 *Phys. Rev. Lett.* **91**, 046402.

Martin, R. M. & Falicov, L. M. 1983 *Light Scattering in Solids. I* (ed. M. Cardona). Topics in Applied Physics, vol. 8, ch. 3, pp. 70–145. Springer.

Maultzsch, J., Reich, S. & Thomsen, C. 2002 *Phys. Rev.* B **65**, 233402.

Milnera, M., Kürti, J., Hulman, M. & Kuzmany, H. 2000 *Phys. Rev. Lett.* **84**, 1324–1327.

Pimenta, M. A., Marucci, A., Empedocles, S., Bawendi, M., Hanlon, E. B., Rao, A. M., Eklund, P. C., Smalley, R. E., Dresselhaus, G. & Dresselhaus, M. S. 1998 *Phys. Rev.* B **58**, R16016–R16019.

Pimenta, M. A., Hanlon, E. B., Marucci, A., Corio, P., Brown, S. D. M., Empedocles, S. A., Bawendi, M. G., Dresselhaus, G. & Dresselhaus, M. S. 2000 *Brazil. J. Phys.* **30**, 423–427.

Rao, A. M., Eklund, P. C., Bandow, S., Thess, A. & Smalley, R. E. 1997a *Science* **275**, 187–191.

Rao, A. M. (and 12 others) 1997b *Nature* **388**, 257–259.

Rao, A. M. *et al.* 2000 *Phys. Rev. Lett.* **84**, 1820–1823.

Saito, R., Dresselhaus, G. & Dresselhaus, M. S. 1998 *Physical properties of single wall carbon nanotubes.* London: Imperial College Press.

Saito, R., Jorio, A., Hafner, J. H., Lieber, C. M., Hunter, M., McClure, T., Dresselhaus, G. & Dresselhaus, M. S. 2001 *Phys. Rev.* B **64**, 085312.

Saito, R., Jorio, A., Souza Filho, A. G., Dresselhaus, G., Dresselhaus, M. S. & Pimenta, M. A. 2002 *Phys. Rev. Lett.* **88**, 027401.

Samsonidze, Ge. G., Saito, R., Jorio, A., Pimenta, M. A., Souza Filho, A. G., Grüneis, A., Dresselhaus, G. & Dresselhaus, M. S. 2003a *J. Nanosci. Nanotechnol.* **3**(6), 431–458.

Samsonidze, Ge. G., Saito, R., Jorio, A., Souza Filho, A. G., Grüneis, A., Pimenta, M. A., Dresselhaus, G. & Dresselhaus, M. S. 2003b *Phys. Rev. Lett.* **90**, 027403.

Small, J. P., Shi, L. & Kim, P. 2003 *Solid State Commun.* **127**, 181–186.

Souza, M. *et al.* 2003 *Phys. Rev.* B **69**, 241403.

Souza Filho, A. G., Jorio, A., Hafner, J. H., Lieber, C. M., Saito, R., Pimenta, M. A., Dresselhaus, G. & Dresselhaus, M. S. 2001 *Phys. Rev.* B **63**, 241404R.

Souza Filho, A. G. (and 11 others) 2002a *Chem. Phys. Lett.* **354**, 62–68.

Souza Filho, A. G. (and 10 others) 2002b *Phys. Rev.* B **65**, 085417.

Souza Filho, A. G., Jorio, A., Samsonidze, Ge. G., Dresselhaus, G., Pimenta, M. A., Dresselhaus, M. S., Swan, A. K., Ünlü, M. S., Goldberg, B. B. & Saito, R. 2003 *Phys. Rev.* B **67**, 035427.

Souza Filho, A. G. *et al.* 2004 *Phys. Rev.* B **69**, 115428.

Sun, H. D. *et al.* 1999 *Solid State Commun.* **109**, 365–369.

Thomsen, C. & Reich, S. 2000 *Phys. Rev. Lett.* **85**, 5214.

Thomsen, C., Reich, S. & Maultzsch, J. 2004 *Phil. Trans. R. Soc. Lond.* A **362**, 2337–2359.

Tohji, K. (and 11 others) 1996 *Nature* **383**, 679.

Wang, N., Tang, Z. K., Li, G. D. & Che, J. S. 2000 *Nature* **408**, 50.

Zhao, Y., Yakobson, B. I. & Smalley, R. E. 2002 *Phys. Rev. Lett.* **88**, 185501.

Zólyomi, V., Kürti, J., Grüneis, A. & Kuzmany, H. 2003 *Phys. Rev. Lett.* **90**, 157401.